

Dirac surface states in intrinsic magnetic topological insulators

EuSn₂As₂ and MnBi₂Te₄

Hang Li,^{1,2,#} Shun-Ye Gao,^{1,2,#} Shao-Feng Duan,^{3,#} Yuan-Feng Xu,^{1,4,#} Ke-Jia Zhu,^{1,2,#}
Shang-Jie Tian,^{5,#} Wen-Hui Fan,^{1,2} Zhi-Cheng Rao,^{1,2} Jie-Rui Huang,^{1,2} Jia-Jun Li,^{1,2}
Zheng-Tai Liu,⁶ Wan-Ling Liu,⁶ Yao-Bo Huang,⁷ Yu-Liang Li,⁸ Yi Liu,⁸ Guo-Bin
Zhang,⁸ He-Chang Lei,⁵ You-Guo Shi,^{1,9} Wen-Tao Zhang,^{3,10,*} Hong-Ming Weng,^{1,2,9,*}
Tian Qian,^{1,9,*} Hong Ding^{1,2,9,11}

¹ *Beijing National Laboratory for Condensed Matter Physics and Institute of Physics, Chinese Academy of Sciences, Beijing 100190, China*

² *University of Chinese Academy of Sciences, Beijing 100049, China*

³ *Key Laboratory of Artificial Structures and Quantum Control (Ministry of Education), School of Physics and Astronomy, Shanghai Jiao Tong University, Shanghai 200240, China*

⁴ *Max Planck Institute of Microstructure Physics, Halle 06120, Germany*

⁵ *Department of Physics and Beijing Key Laboratory of Opto-electronic Functional Materials and Micro-nano Devices, Renmin University of China, Beijing 100872, China*

⁶ *State Key Laboratory of Functional Materials for Informatics, Shanghai Institute of Microsystem and Information Technology (SIMIT), Chinese Academy of Sciences, Shanghai 200050, China*

⁷ *Shanghai Synchrotron Radiation Facility, Shanghai Advanced Research Institute, Chinese Academy of Sciences, 201204 Shanghai, China*

⁸ *National Synchrotron Radiation Laboratory, University of Science and Technology of China, Hefei 230029, China*

⁹ *Songshan Lake Materials Laboratory, Dongguan, Guangdong 523808, China*

¹⁰ *Collaborative Innovation Center of Advanced Microstructures, Nanjing 210093, China*

¹¹ *CAS Center for Excellence in Topological Quantum Computation, University of Chinese Academy of Sciences, Beijing 100049, China*

These authors contributed equally to this work.

* Corresponding authors: tqian@iphy.ac.cn, hmweng@iphy.ac.cn, wentaozhang@sjtu.edu.cn

Abstract

In magnetic topological insulators (TIs), the interplay between magnetic order and nontrivial topology can induce fascinating topological quantum phenomena, such as the quantum anomalous Hall effect, chiral Majorana fermions and axion electrodynamics. Recently, a great deal of attention has been focused on the intrinsic magnetic TIs, where disorder effects can be eliminated to a large extent, which is expected to facilitate the emergence of topological quantum phenomena. In spite of intensive efforts, the experimental evidence of topological surface states (SSs) remains elusive. Here, by combining first-principles calculations and angle-resolved photoemission spectroscopy (ARPES) experiments, we have revealed that EnSn_2As_2 is an antiferromagnetic TI with observation of Dirac SSs consistent with our prediction. We also observed gapless Dirac SSs in another antiferromagnetic TI MnBi_2Te_4 , which were missed in previous ARPES study. These results provide clear evidence for nontrivial topology of the two intrinsic magnetic TIs. Moreover, the topological SSs show no observable changes across the magnetic transitions within the experimental resolution, indicating that the magnetic order has limited effect on the topological SSs, which can be attributed to weak hybridization between the magnetic states and the topological electronic states. This provides insights for further studies that the correlations between magnetism and topological states need to be strengthened to induce larger gaps of the topological SSs, which will facilitate the realization of topological quantum phenomena at higher temperatures.

Time-reversal symmetry has played a key role in topological quantum states of matter. The earliest discovered topological insulator (TI), Chern insulator with the integer quantum Hall effect, requires broken the time-reversal symmetry [1-3]. The thinking and research on time-reversal symmetry in condensed matter systems directly led to the discovery of time-reversal-invariant Z_2 TIs with the quantum spin Hall effect [4-7]. The introduction of magnetism into the Z_2 TIs can produce more exotic topological quantum phenomena, such as the quantum anomalous Hall effect [8-14], axion insulator states [15-21] and chiral Majorana fermions [22].

The quantum anomalous Hall effect has been first realized in magnetically doped $(\text{Bi,Sb})_2\text{Te}_3$ thin films [9,10]. In the magnetically doped TIs, the magnetic impurities usually induce strong inhomogeneity, which is believed to be one of the main reasons that the quantum anomalous Hall effect usually appears at extremely low temperatures (< 100 mK), hindering further exploration of topological quantum effects. A direct solution to avoid disorder is to seek for intrinsic magnetic TIs, which have magnetic order in the stoichiometric compositions.

In the past year, significant progress has been made in this field [16-21,23-39]. Theory has predicted several intrinsic antiferromagnetic (AF) TIs, such as MnBi_2Te_4 [16,19-21,33,40] and EuIn_2As_2 [17], while most experimental studies focused on MnBi_2Te_4 [18,21,25-27,30-39]. Very recently, a quantized Hall plateau at h/e^2 was realized in few-layer MnBi_2Te_4 sheets under moderate magnetic fields of several Tesla [30,32]. The intriguing phenomenon was attributed to a transition from an AF TI to a Chern insulator driven by magnetic fields. The angle-resolved photoemission spectroscopy (ARPES) experiments on MnBi_2Te_4 and MnBi_4Te_7 revealed a large gap of ~ 100 meV in the AF state, which was considered to be associated with the time-reversal symmetry breaking [21,25-29]. However, it is confusing that the large gap remains when the time-reversal symmetry is restored at temperatures much higher than the AF transition temperature [21,25-29]. Another ARPES experiment on EuSn_2P_2 did not obtain information about topological surface states (SSs), because the samples were hole doped with the bulk band gap above the Fermi level (E_F) [24]. In this work, we not only reveal the gapless Dirac SSs of MnBi_2Te_4 within the large gap observed in previous ARPES studies, but also discover another intrinsic magnetic TI EuSn_2As_2 by combining first-principles calculations and ARPES measurements.

EuSn₂As₂ has a layered crystal structure with space group $R\bar{3}m$ [Fig. 1(a)]. Each trigonal Eu layer is sandwiched between two buckled honeycomb SnAs layers. Two adjacent SnAs layers are coupled by van der Waals force. This allows EuSn₂As₂ to be easily exfoliated into few-layer sheets like MnBi₂Te₄ [26,30-32,41]. A previous study has revealed that EuSn₂As₂ undergoes a transition from a paramagnetic (PM) state to an AF state around 25 K [41], which is consistent with our measurements in Figs. 1(b) and 1(c). In the AF state, the Eu 4*f* magnetic moments form an *A*-type AF structure, *i.e.*, ferromagnetic *a-b* planes coupled antiferromagnetically along the *c* axis. In addition, when magnetic fields are perpendicular to the *c* axis, the susceptibility $\chi(T)$ in Fig. 1(b) shows an upturn below 10 K and the isothermal magnetization $M(H)$ at 2 K in Fig. 1(c) increases rapidly at low fields, indicating an in-plane ferromagnetic component probably due to canting of the magnetic moments.

We first analyzed the topological properties of EuSn₂As₂ in the AF state. The Hubbard interaction U on Eu 4*f* electrons was set to be 5 eV in the calculations in Fig. 1(d), in which the energy position of the Eu 4*f* flat bands is consistent with the experimental value (~ 1.7 eV below E_F in Fig. 2(a)). The calculated bands show a continuous gap throughout the Brillouin zone (BZ) near E_F . One can see an anti-crossing feature around Γ , suggesting that EuSn₂As₂ might be topologically nontrivial. The time-reversal symmetry \mathcal{T} is broken in the AF state. However, a combined symmetry $\mathcal{T}\ell_{1/2}$ is preserved, where $\ell_{1/2}$ is a translation operation of half of the magnetic unit cell along the *c* axis, as indicated in Fig. 1(a). This makes $\mathcal{T}\ell_{1/2}$ an antiunitary symmetry operation in the $k_z = 0$ plane, where a Z_2 topological invariant is well defined. We used the Wilson-loop method to calculate the Z_2 invariant. The calculated result in Figs. 1(e) and 1(f) shows a nontrivial winding structure across the BZ in the $k_z = 0$ plane, indicating that EuSn₂As₂ is an AF TI with $Z_2 = 1$, which is consistent with our parity analysis.

For EuSn₂As₂, the formation of magnetic order in the Eu 4*f* states changes the whole symmetry of the system, but does not affect the band inversion of the Sn 5*p* and As 4*p* orbitals near E_F . In the PM state, EuSn₂As₂ is a time-reversal invariant TI with gapless Dirac SSs in the inverted band gap, as confirmed by our experiments below. In the magnetically ordered state, the changes of the Dirac SSs depend on the specific magnetic structures and spin orientations. Figures 1(g) and 1(h) show the calculations

in the A -type AF structure with magnetic moments along the b (AF- b) and c (AF- c) axes, respectively. In both magnetically ordered states, the $\mathcal{T}\ell_{1/2}$ symmetry is broken at the (001) surface, which causes the Dirac SSs to open an energy gap at $\bar{\Gamma}$. However, in the AF- b phase, the vertical mirror plane perpendicular to the magnetic moments is kept. This makes EuSn_2As_2 a topological crystalline insulator characterized by nonzero mirror Chern number of the occupied states within the preserved mirror plane. The mirror symmetry protects a massless Dirac cone deviating from the $\bar{\Gamma}$ point on the line projected by the mirror plane on the (001) surface, as seen in Fig. 1(g). In the AF- c phase, all the vertical mirror symmetries are broken since the magnetic moments are parallel to them. EuSn_2As_2 becomes an axion insulator protected by inversion symmetry, where the Dirac SSs open an energy gap on all surfaces, leaving one-dimensional hinge states between the gapped SSs [17,42]. However, the opened gap at $\bar{\Gamma}$ is too small (< 1 meV) to be resolved in Fig. 1(h). The varying magnetic states with different symmetries lead to various topological states. We draw a schematic diagram in Fig. 1(i) to illustrate the relationship between them, which is similar to the analysis for EuIn_2As_2 [17].

We then investigated the electronic structures on the (001) surface of EuSn_2As_2 with ARPES. The band dispersions measured at different photon energies ($h\nu$) in Fig. 2(b) have no obvious changes. We use the data collected with $h\nu = 29$ eV to illustrate the electronic structures near E_F in Figs. 2(c)-2(e). The data reveal that all near- E_F bands lie around the BZ center $\bar{\Gamma}$. Two hole-like bands (labelled as α and β) form two circular FSs centered at $\bar{\Gamma}$. In addition, one can see a small feature at E_F at $\bar{\Gamma}$ (labelled as γ), which should be the bottom of an electron-like band, and an “M”-shaped band below E_F (labelled as δ). The experimental data are consistent with the calculated valence bands in Fig. 2(f) except for a rigid band shift of ~ 0.18 eV. This suggests that the EuSn_2As_2 samples are hole doped, which is similar to the case of EuSn_2P_2 [24].

For the hole-doped samples, conventional ARPES measurements cannot obtain the information in the band gap. Instead, we used time-resolved ARPES (tr-ARPES) with the pump-probe method to measure the unoccupied electronic states above E_F . In Fig. 3(a), the snapshots of ARPES intensity at different pump-probe delay times reveal Dirac-like band dispersions at ~ 0.4 eV above E_F . To illustrate the topological attribute of the Dirac band, we combine the tr-ARPES data with the conventional ARPES data

in Fig. 3(d). The lower branch of the Dirac band connects to the band α . The bands β and γ connect just above E_F and constitute a single band with an “M” shape. The upper branch of the Dirac band connects to the electron-like conduction band. The experimental results are consistent with our calculations in Fig. 1. The stack of equal-energy contours in Fig. 3(e) show that the Dirac SSs has a cone-like feature, which is rather isotropic.

The single Dirac cone observed at 40 K ambiguously confirms that EuSn_2As_2 is a strong TI in the PM state. As discussed above, the (001) Dirac SSs either open an energy gap or shift slightly off the $\bar{\Gamma}$ point in the AF state. Within our resolution, we did not observe any significant changes in the Dirac SSs between the PM state (40 K) and the AF state (4 K). According to our calculations, the effects of the magnetic order on the Dirac SSs are very small. The main reason is that the correlations between the electronic states involved in the magnetic order and those in the nontrivial topology are too weak. The magnetic moments derive from the Eu 4*f* electronic states, which are very localized and lie at 1.7 eV below E_F . The nontrivial topology is caused by the inversion of the Sn 5*p* and As 4*p* states near E_F . In the AF state, the Eu 4*f* spins form a long-range magnetic order, which breaks the time-reversal symmetry, allowing the surface Dirac bands to hybridize at $\bar{\Gamma}$ to develop an energy gap. The magnitude of hybridization depends on the hopping probability between the Eu 4*f* states and the *p* orbitals related to the nontrivial topology. Since the topological electronic states has little contribution from the Eu 4*f* states, the effects of magnetic order on the Dirac SSs are very limited.

In addition to EuSn_2As_2 , we observed gapless Dirac SSs in MnBi_2Te_4 . Previous ARPES results showed a large gap of ~ 100 meV, in which the spectral intensity has a local minimum [18,21,25-29]. We did observe a band gap of ~ 100 meV, but remarkably, our data reveal an extra electronic state within the gap, showing a peak at -0.28 eV in the energy distribution curves (EDCs) in Fig. 4(e). In order to clarify the band dispersions of the in-gap state, we performed second derivative of the ARPES data with respect to energy. In the intensity maps of second derivative in Figs. 4(c) and 4(d), two bands linearly cross, forming a Dirac point at -0.28 eV. The Fermi velocity of the Dirac fermion is 3.6×10^5 m/s, which is comparable with that in Bi_2Te_3 ($\sim 4 \times 10^5$ m/s).

In the AF state of MnBi_2Te_4 , we did not observe the gap opening at the Dirac point

in Figs. 4(b) and 4(d). This is in contrast to the theoretical calculations that have proposed an energy gap of tens of meV in the AF-*c* phase [19-21,23,40]. The AF-*c* phase of MnBi₂Te₄ has been confirmed by neutron diffraction experiments [35]. In MnBi₂Te₄, the magnetic moments derive from the Mn 3*d* states, and the nontrivial topology is caused by the inversion of the Bi 6*p* and Te 5*p* states near the bulk band gap. In order to clarify the contribution of magnetic Mn 3*d* states to the topological electronic states, we performed resonance photoemission spectroscopy measurements at the Mn 3*p*–3*d* absorption edge. The difference between the on- and off-resonance spectra in Fig. 4(h) reveal that the Mn 3*d* states are mainly located at ~ 4 eV below E_F . In addition, the feature at ~ 1 eV below E_F originates from the hybridization of the Mn 3*d* and Te 5*p* states. However, the component of Mn 3*d* states is negligible in the energy range within 0.6 eV below E_F , where the nontrivial topology arises. This indicates that the hybridization of the Mn 3*d* and the *p* orbitals related to the nontrivial topology is weak. The theoretical calculations may overestimate the effects of the magnetic order on the Dirac SSs even though the Mn 3*d* states are not as localized as the Eu 4*f* states. The inconsistency between experiment and theory calls for further theoretical investigation.

We have observed the gapless Dirac SSs across the bulk band gap of EuSn₂As₂ and MnBi₂Te₄, demonstrating their nontrivial topology. According to our results, the gaps in the AF state should be of the order of meV or less, which can be attributed to weak coupling between the local magnetic moments and the topological electronic states. It is highly desirable to find the intrinsic magnetic TIs in that the topological electronic states are heavily involved in the magnetic order, which may be critical to realize topological quantum phenomena at higher temperatures.

Note added. We become aware of a similar study [43,44] showing the gapless Dirac SSs in MnBi₂Te₄ when finalizing the present paper.

Method

Sample synthesis

Single crystals of EuSn_2As_2 were grown by the Sn flux method at the Institute of Physics, Chinese Academy of Sciences. The high-purity Eu (rod), Sn (shot), and As (lump) were put into corundum crucibles and sealed into quartz tubes with a ratio of $\text{Eu}:\text{As}:\text{Sn} = 1:3:20$. The tubes were heated to $1000\text{ }^\circ\text{C}$ at the rate of $100\text{ }^\circ\text{C}/\text{h}$ and held there for 12 h, then cooled to $750\text{ }^\circ\text{C}$ at a rate of $2\text{ }^\circ\text{C}/\text{h}$. The flux was removed by centrifugation, and shiny crystals were obtained.

Single crystals of MnBi_2Te_4 were grown by the self-flux method at Renmin University of China. The high-purity Mn (piece), Bi (shot) and Te (shot) were put into corundum crucibles and sealed into quartz tubes with a ratio of $\text{Mn}:\text{Bi}:\text{Te} = 1:11.7:18.55$ ($\text{MnTe}:\text{Bi}_2\text{Te}_3 = 1:5.85$). The tube was heated to $950\text{ }^\circ\text{C}$ at a rate of $40\text{ }^\circ\text{C}/\text{h}$ and held there for 12 h, then cooled to $580\text{ }^\circ\text{C}$ at a rate of $10\text{ }^\circ\text{C}/\text{h}$. The flux was removed by centrifugation, and shiny crystals were obtained.

Band structure calculations

EuSn_2As_2 is crystallized in a rhombohedral lattice with space group of $R\bar{3}m$ (No. 166). The experimental lattice constants $a = b = 4.2071\text{ \AA}$ and $c = 26.463\text{ \AA}$ were adopted in our first-principles calculations. The Eu, Sn and As atoms are located at the Wyckoff position $3a(0, 0, 0)$, $6c(0, 0, 0.20963)$ and $6c(0, 0, 0.40624)$, respectively. The Vienna Ab initio Simulation Package (VASP) with the generalized gradient approximation–Perdew, Burke and Ernzerhof (PBE–GGA)-type exchange correlation potential was employed and the BZ sampling was performed by using k grids with an $11\times 11\times 3$ mesh in self-consistent calculations. To match the energy position of Eu $4f$ bands in experiments, the Hubbard U parameter of the $4f$ electrons was taken as 5 eV in the GGA+ U calculations. We have generated the maximally localized Wannier functions for the $5s$ and $5p$ orbitals on Sn and the $4p$ orbitals on As using the WANNIER90 package. The surface states calculations were performed using the Green’s function method based on the Wannier Tools package.

Synchrotron angle-resolved photoemission spectroscopy

ARPES measurements on EuSn_2As_2 were performed at the “CASSIOPEE”

beamline, SOLEIL, France, with a Scienta R4000 analyzer, and the “dreamline” beamline at the Shanghai Synchrotron Radiation Facility (SSRF) with a Scienta DA30 analyzer. ARPES measurements on MnBi_2Te_4 were performed at the 03U beamline at the Shanghai Synchrotron Radiation Facility (SSRF) and at the 13U beamline at the National Synchrotron Radiation Laboratory at Hefei with Scienta DA30 analyzers.

Time-resolved angle-resolved photoemission spectroscopy

The tr-ARPES experiments were performed at Shanghai Jiao Tong University. In tr-ARPES measurements, infrared photon pulses with wavelength centered at 700 nm (1.77 eV) and pulse length of 30 fs were used to excite the sample, and the non-equilibrium states were probed by ultraviolet pulses at 205 nm (6.05 eV). Photoelectrons were collected by a Scienta DA30L-8000R analyzer. The overall time resolution and energy resolution are 130 fs and 19 meV respectively [45]. Sample was cleaved at a pressure better than 3×10^{11} torr at 4 K.

Acknowledgements

T.Q. thanks Kun Jiang for discussions. This work was supported by the Ministry of Science and Technology of China (2016YFA0300600, 2018YFA0305700, 2016YFA0300500, 2017YFA0302901, and 2016YFA0401000), the National Natural Science Foundation of China (11622435, U1832202, 11674369, 11674224, 11774399, 11574394, 11774423, 11822412 and 11888101), the Chinese Academy of Sciences (QYZDB-SSW-SLH043 and XDB28000000), the Fundamental Research Funds for the Central Universities, the Research Funds of Renmin University of China (15XNLQ07, 18XNLG14 and 19XNLG17), the Beijing Municipal Science & Technology Commission (Z171100002017018, Z181100004218001 and Z181100004218005), the Beijing Natural Science Foundation (Z180008), the Science Challenge Project (TZ2016004), and the K. C. Wong Education Foundation (GJTD-2018-01).

Reference

- [1] K. v. Klitzing, G. Dorda, M. Peper, *New method for high-accuracy determination of the fine-structure constant based on quantized Hall resistance*, Phys. Rev. Lett. **45**, 494 (1980).
- [2] D. J. Thouless, M. Kohmoto, M. P. Nightingale, and M. den Nijs, *Quantized Hall Conductance in a Two-Dimensional Periodic Potential*, Phys. Rev. Lett. **49**, 405 (1982).
- [3] F. D. M. Haldane, *Fractional Quantization of the Hall Effect: A Hierarchy of Incompressible Quantum Fluid States*, Phys. Rev. Lett., **51**, 605 (1983).
- [4] F. D. M. Haldane, *Model for a quantum Hall effect without Landau levels: condensed-matter realization of the ‘parity anomaly’*, Phys. Rev. Lett. **61**, 2015 (1988).
- [5] S. Murakami, N. Nagaosa and S.-C. Zhang, *Spin-Hall insulator*, Phys. Rev. Lett. **93**, 156804 (2004).
- [6] C. L. Kane and E. J. Mele, *Z_2 topological order and the quantum spin Hall effect*, Phys. Rev. Lett. **95**, 146802 (2005).
- [7] L. Fu, C. L. Kane, *topological insulators with inversion symmetry*, Phys. Rev. B **76**, 045302 (2007).
- [8] R. S. K. Mong, A. M. Essin, and J. E. Moore, *Antiferromagnetic topological insulators*, Phys. Rev. B **81**, 245209 (2010).
- [9] R. Yu, et al., *Quantized Anomalous Hall Effect in Magnetic Topological Insulators*, Science **329**, 61 (2010).
- [10] C.-Z. Chang, et al., *Experimental Observation of the Quantum Anomalous Hall Effect in a Magnetic Topological Insulator*, Science **340**, 167 (2013).
- [11] J. Wang, B. Lian, and S.-C. Zhang, *Quantum anomalous Hall effect in magnetic topological insulators*, Phys. Scr. **T164**, 014003 (2015).
- [12] J. G. Checkelsky, et al., *Trajectory of the anomalous Hall effect towards the quantized state in a ferromagnetic topological insulator*, Nat. Phys. **10**, 731 (2014).
- [13] X.-F. Kou, et al., *Scale-invariant quantum anomalous Hall effect in magnetic topological insulators beyond the two-dimensional limit*, Phys. Rev. Lett. **113**, 137201

(2014).

[14] C.-Z. Chang, et al., *High-precision realization of robust quantum anomalous Hall state in a hard ferromagnetic topological insulator*, Nat. Mater. **14**, 473 (2015).

[15] M. Mogi, et al., *A magnetic heterostructure of topological insulators as a candidate for an axion insulator*, Nat. Mater. **16**, 516 (2017).

[16] D.-Q. Zhang, et al., *Topological axion states in magnetic insulator $MnBi_2Te_4$ with the quantized magnetoelectric effect*, Phys. Rev. Lett. **122**, 206401 (2019).

[17] Y.-F. Xu, Z.-D. Song, Z.-J. Wang, H.-M. Weng and X. Dai, *Higher-Order Topology of the Axion Insulator $EuIn_2As_2$* , Phys. Rev. Lett. **122**, 256402 (2019).

[18] Y. Gong, et al., *Experimental Realization of an Intrinsic Magnetic Topological Insulator*, Chin. Phys. Lett. **36**, 7 076801 (2019).

[19] J.-H. Li, et al., *Magnetically Controllable Topological Quantum Phase Transitions in Antiferromagnetic Topological Insulator $MnBi_2Te_4$* , arXiv:1905.00642.

[20] M. M. Otrokov, et al., *Unique Thickness-Dependent Properties of the van der Waals Interlayer Antiferromagnet $MnBi_2Te_4$ Films*, Phys. Rev. Lett. **122**, 107202 (2019).

[21] M. M. Otrokov, et al., *Prediction and observation of the first antiferromagnetic topological insulator*, arXiv:1809.07389.

[22] X.-L. Qi, T. L. Hughes and S.-C. Zhang, *Chiral topological superconductor from the quantum Hall state*, Phys. Rev. B **82**, 184516 (2010).

[23] H.-Y. Sun, et al., *Rational design principles of quantum anomalous Hall effect from superlattice-like magnetic topological insulators*, arXiv:1905.12208.

[24] X. Gui, et al., *A New Magnetic Topological Quantum Material Candidate by Design*, arXiv:1903.03888.

[25] R. C. Vidal, et al., *Massive Dirac fermion at the surface of the van der Waals antiferromagnet $MnBi_2Te_4$* , arXiv:1903.11826.

[26] B. Chen, et al., *Searching the $Mn(Sb, Bi)_2Te_4$ family of materials for the ideal intrinsic magnetic topological insulator*, arXiv:1903.09934.

[27] S. H. Lee, et al., *Spin scattering and noncollinear spin structure-induced intrinsic*

anomalous Hall effect in antiferromagnetic topological insulator MnBi₂Te₄, arXiv:1812.00339.

[28] C.-W. Hu, et al., *A van der Waals antiferromagnetic topological insulator with weak interlayer magnetic coupling*, arXiv:1905.02154.

[29] J.-Z. Wu, et al., *Natural van der Waals Heterostructures with Tunable Magnetic and Topological States*, arXiv:1905.02385.

[30] Y.-J. Deng, et al., *Magnetic-field-induced quantized anomalous Hall effect in intrinsic magnetic topological insulator MnBi₂Te₄*, arXiv:1904.11468.

[31] S. Zhang, et al., *Experimental observation of the gate-controlled reversal of the anomalous Hall effect in the intrinsic magnetic topological insulator MnBi₂Te₄ device*, arXiv:1905.04839.

[32] C. Liu, et al., *Quantum phase transition from axion insulator to Chern insulator in MnBi₂Te₄*, arXiv:1905.00715.

[33] J.-H. Li, et al., *Intrinsic magnetic topological insulators in van der Waals layered MnBi₂Te₄-family materials*, Sci. Adv. **5**, eaaw5685 (2019).

[34] J.-H. Cui, et al., *Transport properties of thin flakes of the antiferromagnetic topological insulator MnBi₂Te₄*, Phys. Rev. B **99**, 155125 (2019).

[35] J.-Q. Yan, et al., *Crystal growth and magnetic structure of MnBi₂Te₄*, Phys. Rev. Mater. **3**, 064202 (2019).

[36] P. Rani, et al., *Crystal Growth and basic transport and magnetic properties of MnBi₂Te₄*, arXiv:1906.09038.

[37] A. Zeugner, et al., *Chemical Aspects of the Antiferromagnetic Topological Insulator MnBi₂Te₄*, Chem. Mater. **31**, 2795 (2019).

[38] J.-Q. Yan, et al., *Evolution of structural, magnetic and transport properties in MnBi_{2-x}Sb_xTe₄*, arXiv:1905.00400.

[39] K.-Y. Chen, et al., *Suppression of the antiferromagnetic metallic state in the pressurized MnBi₂Te₄ single crystal*, arXiv:1907.01760.

[40] M. M. Otrokov, et al., *Magnetic Extension as an Efficient Method for Realizing*

the Quantum Anomalous Hall State in Topological Insulators, JETP Letters, **105**, 5, 297 (2017).

[41] M. Q. Arguilla, et al., *EuSn₂As₂: An Exfoliatable Magnetic Layered Zintl-Klemm Phase*, Inorg. Chem. Front. **4**, 378 (2016).

[42] N. Varnava and D. Vanderbilt, *Surfaces of axion insulators*, Phys. Rev. B **98**, 245117 (2018).

[43] Y.-J. Hao, et al., *Gapless surface Dirac cone in antiferromagnetic topological insulator MnBi₂Te₄*, arXiv:1907.03722.

[44] Y.-J. Chen, et al., *Topological Electronic Structure and Its Temperature Evolution in Antiferromagnetic Topological Insulator MnBi₂Te₄*, arXiv:1907.05119.

[45] Y. Y. Yang, et al., *A time- and angle-resolved photoemission spectroscopy with probe photon energy up to 6.7 eV*, Rev. Sci. Instrum. **90**, 063905 (2019).

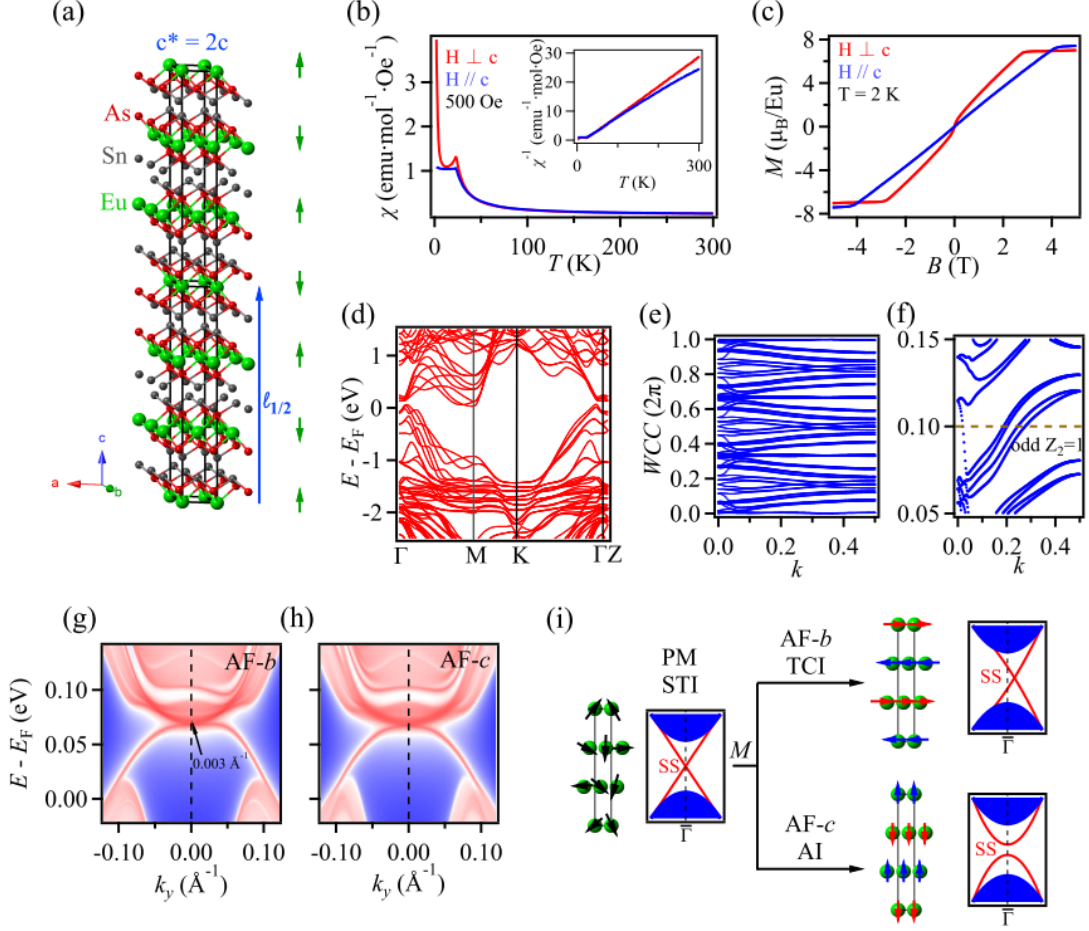


Fig. 1. Magnetic and topological properties of EuSn_2As_2 . (a) Crystal structure of EuSn_2As_2 . The green arrows represent the magnetic moments of Eu atoms, forming a doubled magnetic unit cell $c^* = 2c$. The blue arrow represents the half translation operator $\ell_{1/2}$ of the magnetic unit cell along the c axis. (b) Magnetic susceptibility as a function of temperature under a magnetic field of 500 Oe perpendicular (red) or parallel (blue) to the c axis. The inset shows the inverse susceptibility. (c) Field-dependent magnetization at 2 K with magnetic fields perpendicular (red) or parallel (blue) to the c axis. (d) Calculated bulk band structure of EuSn_2As_2 in the AF state along high-symmetry lines with spin-orbit coupling. (e) Wannier charge centers (WCC) calculated in the time-reversal invariant $k_z = 0$ plane. (f) Zoom-in WCC in (e), confirming $Z_2 = 1$. (g),(h) Calculated band dispersions of (001) SSs and projected bulk states along $\bar{M}-\bar{\Gamma}-\bar{M}$ near the bulk band gap in the AF- b and AF- c phases, respectively. (i) Schematic diagram of topological states of EuSn_2As_2 in three prototypical magnetic phases (PM, AF- b , AF- c). STI, TCI, and AI are the abbreviations of strong topological insulator, topological crystalline insulator, and axion insulator, respectively.

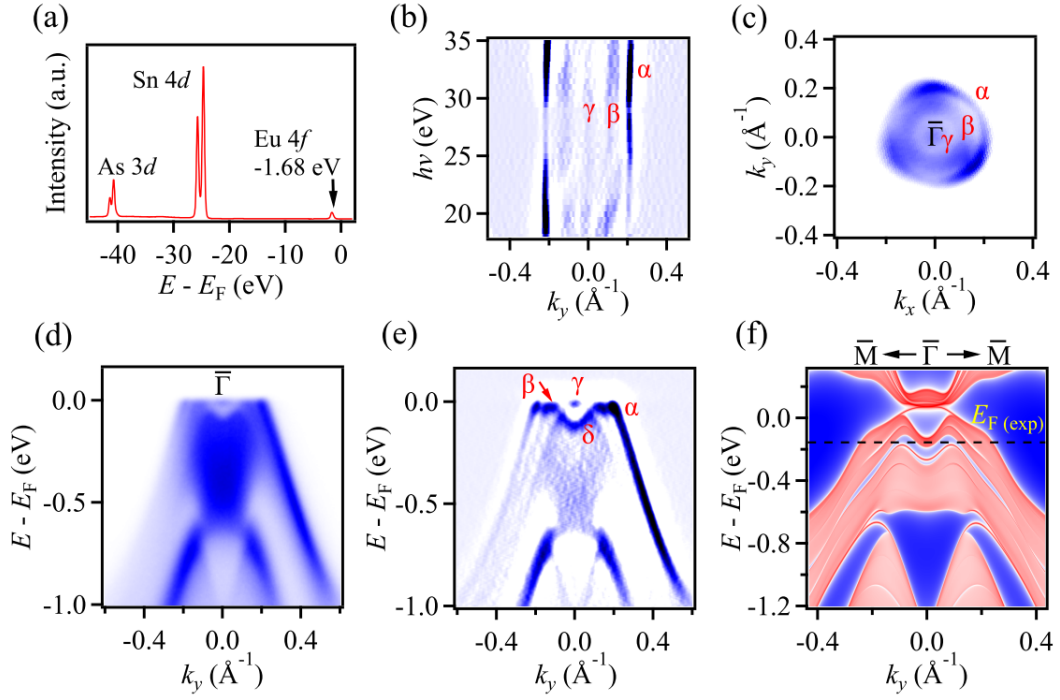


Fig. 2. Electronic structures of the occupied states of EuSn₂As₂. (a) Core-level photoemission spectrum showing the characteristic peaks of As 3*d*, Sn 4*d*, and Eu 4*f* orbitals. (b) Curvature intensity map of the ARPES data at E_F measured in a range of $h\nu$ from 18 to 35 eV. (c) ARPES intensity map around $\bar{\Gamma}$ at E_F . (d) ARPES intensity map along $\bar{M}-\bar{\Gamma}-\bar{M}$. (e) Curvature intensity map of the data in (d). (f) Calculated band dispersions of (001) SSs and projected bulk states along $\bar{M}-\bar{\Gamma}-\bar{M}$. The ARPES data in (c) and (d) were measured at $h\nu = 29$ eV.

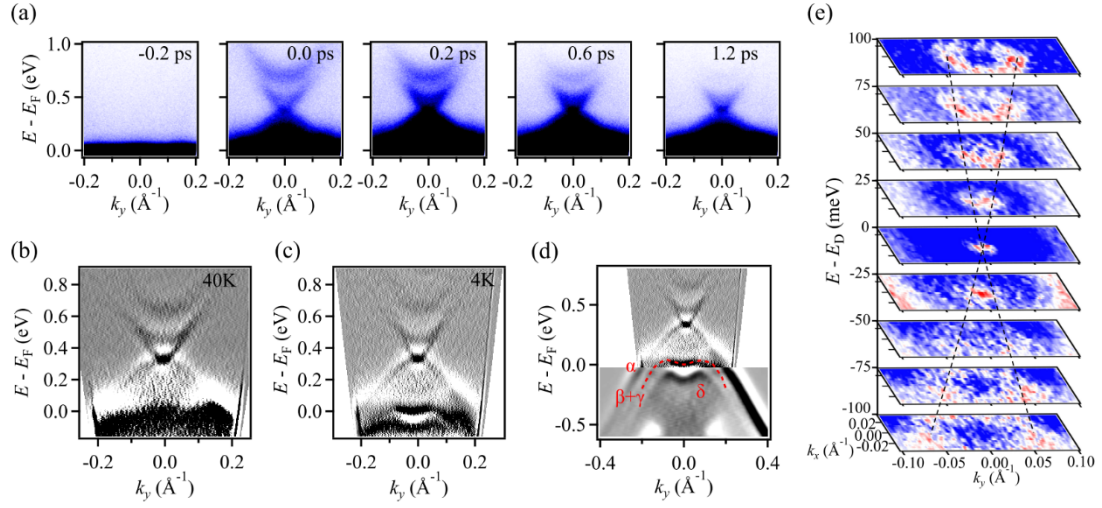


Fig. 3. Surface Dirac cone in the unoccupied states of EuSn₂As₂. (a) Snapshots of the tr-ARPES intensity along $\bar{M}-\bar{\Gamma}-\bar{M}$ measured with the pump-probe method at different delay times. (b),(c) Curvature intensity maps of the pump-probe data at the delay time 0.2 ps measured at 40 and 4 K, respectively. (d) Combination of the data in Fig. 3(c) and Fig. 2(e). (e) Stack of curvature intensity maps of the pump-probe data at different constant energies. The energy of the Dirac point (E_D) is set to zero.

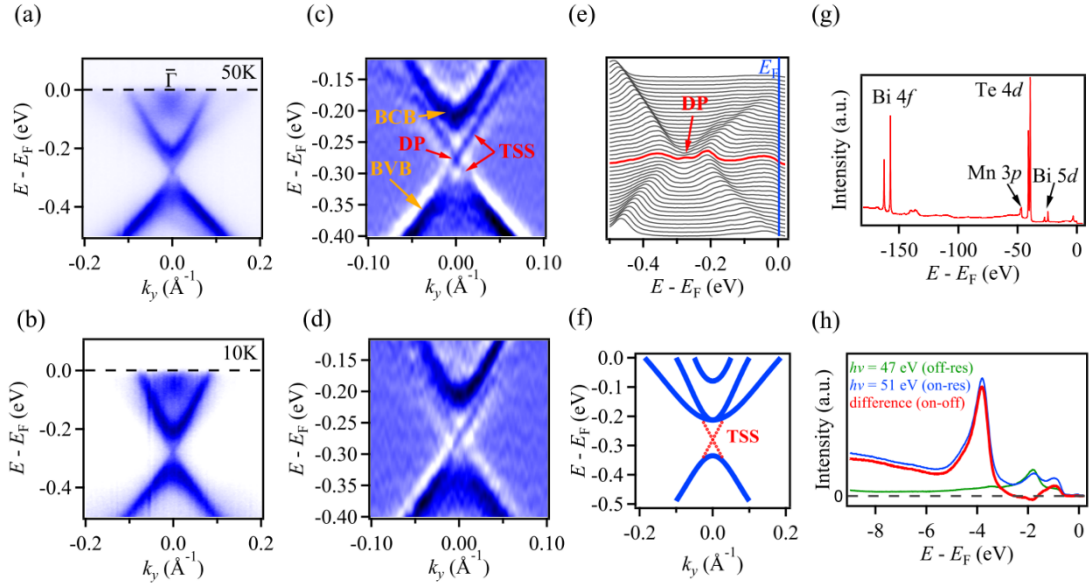


Fig. 4. (001) Dirac SSs of MnBi₂Te₄. (a),(b) ARPES intensity maps of MnBi₂Te₄ at 50 K and 10 K, respectively. (c),(d) Intensity maps of second derivative with respect to energy of the data near the bulk band gap in a and b, respectively. TSS, DP, BCB and BVB are the abbreviations of topological surface states, Dirac point, bulk conduction band, and bulk valence band, respectively. (e) EDCs around the Dirac point of the data in (a). The red curve indicates the EDC at $\bar{\Gamma}$. (f) Band dispersions extracted from the data in (a). Blue lines and red dots represent the bulk states and topological surface states, respectively. (g) Core-level photoemission spectrum showing the characteristic peaks of Bi 4f, Bi 5d, Mn 3p, and Te 4d orbitals. (h) Resonant valence band spectra of MnBi₂Te₄ taken at the Mn 3p-3d absorption edge. On and off-resonance spectra were obtained at $h\nu = 51$ and 47 eV, respectively. The ARPES data in (a) and (b) were measured at $h\nu = 13.8$ eV.